Journal of Controlled Release 319 (2020) 407–415

Contents lists available at ScienceDirect

Journal of Controlled Release

journal homepage: www.elsevier.com/locate/jconrel

Transferrin-binding peptide functionalized polymersomes mediate targeted doxorubicin delivery to colorectal cancer *in vivo*

Yaohua Wei[a,b], Xiaolei Gu[a], Yinping Sun[a], Fenghua Meng[a,*], Gert Storm[b], Zhiyuan Zhong[a,*]

[a] Biomedical Polymers Laboratory, College of Chemistry, Chemical Engineering and Materials Science, State Key Laboratory of Radiation Medicine and Protection, Soochow University, Suzhou 215123, PR China

[b] Department of Biomaterials Science and Technology, MIRA Institute for Biological Technology and Technical Medicine, University of Twente, PO Box 217, 7500AE Enschede, the Netherlands

ARTICLE INFO

Keywords:
Transferrin
Polymersomes
Targeted delivery
Colorectal cancer
Chemotherapy

ABSTRACT

Transferrin receptor (TfR) is a promising target validated in the clinical trials for managing various malignancies. Transferrin (Tf) and single chain antibody fragment can target TfR and are typically conjugated to nanomedicines *via* post-modification, which poses significant production challenges. Here, we report that the polymersomes functionalized with a Tf-binding peptide CGGGHKYLRW (TBP-Ps) can selectively and stably bind Tf and subsequently mediate targeted doxorubicin (Dox) delivery to TfR over-expressing HCT-116 colorectal cancer cells *in vitro* and *in vivo*. The Tf surface density of the polymersomes could be controlled by the surface content of TBP. Interestingly, modifying Dox-loaded TBP-Ps with Tf led to greatly increased cellular uptake and inhibitory effect of HCT-116 cells. Tf-bound TBP-Ps demonstrated rapid accumulation in the tumor xenografts in nude mice following *i.v.* injection. More importantly, Dox-loaded Ps with Tf binding significantly enhanced the antitumor efficacy in mice bearing HCT-116 tumors compared to polymersomes without Tf binding. Surface functionalization of the nanoparticles with Tf-binding peptide provides an appealing strategy in formulating Tf-targeted nanomedicines.

1. Introduction

Targeted nanomedicines are considered as a future treatment modality for cancers [1–4]. To accomplish targeted delivery, researchers have decorated nanomedicines with different ligands ranging from peptides [5,6], antibodies [7] and antibody fragments [8], glycoproteins [9–11], to folic acid [12,13]. In spite of intensive investigations, few actively targeted nanomedicines have come to the stage of clinical translation [14–16]. Notably, several targeted nanoformulations homing to transferrin receptor (TfR) have been approved for clinical trials [17–19]. TfR over-expresses on highly proliferative cancer cells [10,12,20]. Transferrin (Tf) and single-chain antibody fragment (ScFv) against TfR have been selected as ligands for TfR targeting [21–25]. For example, Davis et al. described that Tf-conjugated, cyclodextrin polymer-based nanoparticles exhibited an enhanced transfection of K562 leukemia cells as compared to the non-targeted control [26], and evidence of RNAi in a phase I clinical trial targeted delivery of siRNA to patients with solid tumor [27]. Chang et al. reported that liposomes modified with ScFv could mediate targeted delivery of wild-type p53 gene to metastatic pancreatic tumor. The results from phase I clinical trial revealed the accumulation of p53 gene in advanced solid tumor in patients, low adverse effects, and stablized disease [28]. However, the conjugation of large ligands like Tf and ScFv to nanomedicines *via* post-modification may pose significant production challenges. The post-modification with large ligands may encounter issues like poor control over conjugation site and efficacy, and difficulty in purification and in scaling up production.

In contrast to large glycoproteins and antibody fragments, peptides with a short sequence and easy handling enable functionalization of nanomedicines *via* pre-modification [29]. Various peptides have been screened as antibody alternatives for targeted tumor therapy in the past years [30–35]. Nevertheless, to date, only BIND-014, a docetaxel nanoformulation decorated with prostate-specific membrane antigen-targeting peptide, has reached clinical assessments [36]. The slow development of peptide-targeted nanomedicines is likely due to the fact that peptides are not as specific and effective as antibodies for *in vivo* targeting. Interestingly, Signore et al. reported that CGGGHKYLRW as a Tf-binding peptide (TBP) showed a high specificity and affinity to Tf [37]. TBP following plasma incubation could promote TfR-mediated cellular uptake of gold nanoparticles.

* Corresponding authors.
E-mail addresses: fhmeng@suda.edu.cn (F. Meng), zyzhong@suda.edu.cn (Z. Zhong).

https://doi.org/10.1016/j.jconrel.2020.01.012
Received 3 August 2019; Received in revised form 30 December 2019; Accepted 6 January 2020
Available online 07 January 2020
0168-3659/

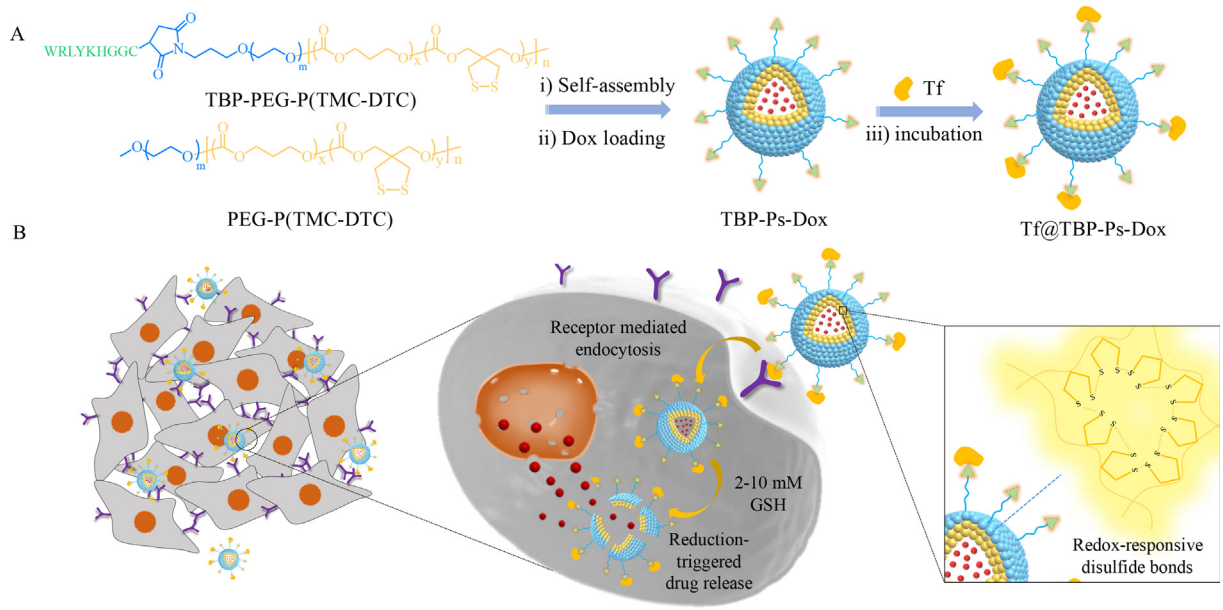

Scheme 1. (A) Schematic of facile fabrication of transferrin-bound polymersomal doxorubicin *via* a transferrin-binding peptide (TBP), CGGGHKYLRW. (i) TBP-functionalized polymersomes (TBP-Ps) are assembled from PEG-P(TMC-DTC) and TBP-PEG-P(TMC-DTC); (ii) Efficient Dox loading into TBP-Ps gives TBP-Ps-Dox *via* a pH-gradient method; and (iii) incubation with transferrin yields transferrin-bound polymersomal doxorubicin (Tf@TBP-Ps-Dox). (B) Tf@TBP-Ps-Dox can not only increase the accumulation and retention in transferrin receptor over-expressing HCT-116 colorectal tumor cells but also enhance the cellular uptake compared to Ps-Dox, leading to enhanced efficacy of targeted therapy of colorectal cancer *in vivo*.

Here, we report for the first time that Tf-binding peptide-functionalized polymersomes (TBP-Ps) loaded with doxorubicin hydrochloride (TBP-Ps-Dox) following Tf binding could mediate targeted Dox delivery to TfR over-expressing HCT-116 colorectal cancer cells *in vitro* and *in vivo* (Scheme 1). Several reports demonstrated that colorectal cancers over-express TfR [38,39]. We previously reported that the disulfide-crosslinked polymersome is a promising substitute to liposome for Dox delivery [40–43]. Interestingly, TBP-Ps-Dox following Tf binding (Tf@TBP-Ps-Dox) revealed greatly enhanced cellular uptake and anti-tumor effect in HCT-116 cells over Ps-Dox. The pharmacokinetics and anti-tumor therapy experiments revealed that Tf@TBP-Ps-Dox exhibited a long circulation time and a considerably improved inhibition of HCT-116 tumor as compared to Ps-Dox. Surface functionalization of the nanoparticles with Tf-binding peptide thus provides an appealing strategy to fabricate nanomedicines targeting to TfR over-expressing malignancies.

2. Experimental methods

2.1. Synthesis of TBP-PEG-P(TMC-DTC)

Poly(ethylene glycol)-*b*-poly(trimethylene carbonate-*co*-dithiolane trimethylene carbonate) (mPEG-P(TMC-DTC)) and maleimide functionalized copolymer Mal-PEG-P(TMC-DTC) were produced according to our previous report (Table S1) [40]. Mal-PEG-P(TMC-DTC) (200 mg, 8.2 μmol) was added under stirring to 1.5 mL TBP (CGGGHKYLRW, 19.2 mg, 16.4 μmol) solution in *N, N*-dimethlyformamide (DMF). The reaction proceeded at 37 °C for 24 h, followed by intensive dialysis (MWCO 3500) against 100 mL DMF (× 3) and 100 mL DCM (× 2) at room temperature (rt) with solvent replacement each hour. TBP-PEG-P(TMC-DTC) was then purified by precipitation in 30-fold cold diethyl ether, filtration and vacuum drying. Yield: 92%. BCA assay was used to determine the conjugation efficiency of TBP as described [44]. The conjugation efficiency was *ca.* 95%.

2.2. Fabrication of TBP-Ps-Dox and Tf@TBP-Ps-Dox

Transferrin binding peptide functionalized polymersomes (TBP-Ps) were co-assembled from TBP-PEG-P(TMC-DTC) and mPEG-P(TMC-DTC). The pH-gradient method was used to obtain doxorubicin hydrochloride (Dox·HCl) loaded polymersomes (TBP-Ps-Dox) [41]. In a typical example, 100 μL DMF solution (40 mg/mL) of mPEG-P(TMC-DTC) and TBP-PEG-P(TMC-DTC) (4/1) was added into 900 μL citrate buffer (pH 4.0, 10 mM) under stirring. After 1 h incubation, saturated Na_2HPO_4 solution was used to adjust the pH to 7.8. To reach a theoretical drug loading content of 16.7 wt%, 160 μL Dox·HCl in deionized solution (5 mg/mL) was added dropwise, and incubated at 37 °C for 12 h before purification by passing G-25 column using phosphate buffer (PB, pH 7.4,10 mM) as an eluent. The polymersomes were collected and concentrated by repeated ultrafiltration (MWCO 10,000 Da, 2600 × g, 10 min, rt). By manipulating the molar ratios of the two copolymers, TBP-Ps-Dox with different surface densities of TBP were produced. Size, size distribution and zeta potential were measured. The DOX loading was quantified using UV–Vis spectroscopy (Ex. 480 nm) [40].

Tf@TBP-Ps was obtained by incubating TBP-Ps with Tf containing solutions. Typically, 1 mL TBP-Ps with TBP molar surface density of 8.6%, 17.2%, and 25.8% referring to total copolymers (4 mg/mL) was incubated with 13.4, 26.8, and 40.2 μM Tf (corresponding to a TBP/Tf molar ratio of 1/1) for 1 h, respectively, followed by 2 times ultrafiltration using ultrafiltration centrifugal tubes (MWCO 100,000 Da, 2600 × g, 10 min, rt). BCA assay was used to determine the Tf surface contents. The influence of incubation time of TBP-Ps with Tf at a concentration in the blood (2 mg/mL) on the final Tf surface contents were also investigated. The size and zeta potential of TBP-Ps-Dox before and after Tf binding were measured.

2.3. Determination of Tf binding stability of Tf@TBP-Ps using ^{125}I labeling

To evaluate the stability of Tf binding to TBP-Ps, Tf was labeled with radioactive ^{125}I. Briefly, into 200 μL of Tf solution in PBS (10 mg/mL) was added 200 μCi of $Na^{125}I$ and 10 μL chloramine-T (10 mg/mL) under constant stirring at rt. After 10 min, ^{125}I-Tf was purified by

ultrafiltration (MWCO 10,000 Da, 3000 rpm, 20 min) to remove free $Na^{125}I$. The final radioactivity of ^{125}I-Tf was measured using gamma counter (GC-1500, USTC ZONKIA, China), and the efficiency of radio labeling was calculated to be *ca.* 100%. Next, a mixture of ^{125}I-Tf/Tf (1/10, mol/mol) was incubated with TBP-Ps for 1 h at predetermined ratios to yield ^{125}I-Tf bound polymersomes (^{125}I-Tf@TBP-Ps). The unbound Tf and ^{125}I-Tf were removed by repeated ultrafiltration (MWCO 100,000 Da, 2600 ×g, 10 min, rt) until no radioactivity could be detected in the filtrate. To determine the Tf binding stability to TBP-Ps, 100 μL of ^{125}I-Tf@TBP-Ps was incubated for 48 h with 400 μL PBS, PB solution containing 20-fold excess Tf, human serum, or mouse whole blood before ultrafiltration (MWCO 100,000 Da, 2600 ×g, 10 min, rt). The radioactivity of the purified ^{125}I-Tf@TBP-Ps was measured and was compared to their radioactivity after 2-day attenuation.

2.4. In vitro cytotoxicity of Tf@TBP-Ps-Dox and blank Tf@TBP-Ps

The studies were conducted using TfR-overexpressing HCT-116 colorectal cancer cells. In brief, the cells seeded in a 96 well plate (3×10^3 cells/well) for 24 h were treated with 20 μL of Tf@TBP-Ps-Dox (5 μg Dox/mL) with varied TBP molar surface densities (0, 8.6%, 17.2%, or 25.8 mol%). The medium was replaced after 2 h incubation prior to another 70 h incubation. Then 3-(4,5-dimethythiazol-2-yl)-2,5-diphenyltetrazoliumbromide (MTT) was added (10 μL, 5 mg/mL) and incubated for 4 h. The culture media were discarded and 150 μL DMSO was incubated for 10 min. The absorbance at 492 nm of each well was acquired, and the cell viability (%) was obtained by comparing the absorbance of the cells treated with PBS only.

The cytotoxicity of Tf@TBP-Ps-Dox with 4.0 mol% Tf to HCT-116 cells in the presence or absence of 20-fold excess Tf (1 mg/mL) was determined using MTT assays, and the Dox concentrations varied from 0.001 to 40 μg/mL. The half-maximal inhibitory concentration (IC_{50}) was derived. Ps-Dox and commercial liposomal doxorubicin (Lipo-Dox) were used as controls. The cytotoxicity of blank Tf@TBP-Ps was similarly conducted with polymer concentrations ranging from 0.1 to 1 mg/mL at 48 h incubation with HCT-116 cells.

Live/dead assays of the cells were performed using a cell double staining kit (Sigma Aldrich) according to the instruction with slight change. Briefly, 10 μL Solution A and 5 μL Solution B were added to 5 mL PBS to prepare an assay solution. HCT-116 cells on microscope coverslips in 24-well plate (1×10^5 cells/well) were washed (PBS, ×3) to remove residual esterase before the incubation with the assay solution (100 μL) for 15 min at 37 °C. After PBS washing (×3), the cells were imaged by fluorescence microscopy (Olympus BX41).

2.5. Cellular uptake and intracellular Dox delivery of Tf@TBP-Ps-Dox

HCT-116 cells in a 6-well plate (3×10^6 cells/well) were cultured for 24 h to achieve 70% confluence. Then, 100 μL of Tf@TBP-Ps-Dox with various TBP surface densities (8.6%, 17.2%, 25.8 mol%) and Ps-Dox were added (10 μg Dox/mL). The cells following 2 h incubation at 37 °C were digested by trypsin (0.25%, w/v) containing EDTA (0.03%, w/v). The suspensions were centrifuged, re-dispersed in 500 μL PBS following twice PBS washing and analyzed using a BD FACS Calibur flow cytometer (ex. 488 nm, em. 560 nm). The competitive inhibition of the internalization of Tf@TBP-Ps-Dox with 17.2 mol% TBP by HCT-116 cells in the presence of 20-fold excess Tf (1 mg/mL) was further studied.

For confocal laser scanning microscopy (CLSM) observation, HCT-116 cells were cultured on microscope coverslips in 24-well plate (1×10^5 cells/well) for 24 h. 100 μL of Tf@TBP-Ps-Dox with 17.2 mol % TBP was added (10 μg Dox/mL) and incubated for 2 h at 37 °C. The cells were washed with PBS and fixed with 4% paraformaldehyde solution for 15 min followed by washing (PBS, ×3). Finally, 4, 6-Diamidino-2-phenylindole solution (DAPI, 5 μg/mL) was added to stain the cell nuclei for 5 min at rt. before acquiring the fluorescence images using CLSM (TCS SP5) with 200 Hz speed, 1024 × 1024 resolution and 13% of Argon laser power.

A live-cell imaging system (CELL'R, Olympus) was used for Dox intracellular trafficking to visualize the internalization and intracellular release in HCT-116 cells. Briefly, the cells were seeded (2×10^5 cells/well) in a glass petri dish (Φ 35 mm) in 900 μL culture medium and incubated with 100 μL Tf@TBP-Ps-Dox with 17.2 mol% TBP or Ps-Dox (10 μg Dox/mL). The fluorescent images were captured at excitation wavelengths of 480 nm every minute.

2.6. TfR expression on HCT-116 cells

The expression of TfR on HCT-116 cell lines was evaluated by labeling with antibody CD71-PE (Miltenyi Biotec) using flow cytometry (MDA-MB 231 cells as positive control). Briefly, the cell suspension was centrifuged at 300 ×*g* for 10 min, and resuspended in PBS at 10^7 cells/100 μL. Then 10 μL of CD71-PE was added to incubate for 10 min at 4 °C in the dark. The cells were then washed by PBS and centrifuged. The supernatant was removed and the cell pellet was resuspended in 500 μL PBS for flow cytometry analysis.

2.7. The pharmacokinetics, in vivo imaging and biodistribution

All animals were handled under protocols approved by Soochow University Laboratory Animal Center and the Animal Care and Use Committee of Soochow University. For the pharmacokinetic studies, 200 μL of Tf@TBP-Ps-Dox or Ps-Dox at 8 mg Dox/kg was injected intravenously (*iv*) to healthy Balb/c mice ($n = 3$). About 50 μL blood was collected from retro-orbital sinus of mice at varied time intervals and 20 μL plasma was used for following study. 500 μL of DMF solution containing 20 mM DTT was added to extract Dox at 25 °C overnight followed by centrifugation. Dox concentration in the supernatant was quantified using fluorometry (ex. 480 nm, em. 560 nm), and was plotted as a function of the time. The half-lives of circulation and the area under curve (AUC) were derived by using second-order exponential decay fit (Prism).

Female Balb/c nude mice (5 weeks) were inoculated with 50 μL HCT-116 cells (1×10^6 cells) on the right hind flank to build subcutaneous tumor model. When tumors grew to ca 150–200 mm^3, 200 μL of Cy5-labeled Tf@TBP-Ps or Ps (75 μg Cy5 equiv./kg) were *iv* administrated into the mice *via* tail veins. The near-infrared images of the mice were acquired at designated time intervals. At 24 h post-injection, the mice were sacrificed, and the major organs and tumors were excised for the *ex vivo* NIR imaging.

For quantification of *in vivo* biodistribution, the mice bearing HCT-116 tumors of 150 mm^3 were *iv* administrated with Tf@TBP-Ps-Dox and Ps-Dox at 8 mg Dox equiv./kg ($n = 3$). After 24 h, the major organs and tumors were excised, and 0.1 g of each tissue was homogenized in Triton (1%, 0.5 mL). 1 mL DMF containing 20 mM DTT was added to extract Dox overnight. After centrifugation, Dox fluorescence in the supernatant was measured using a plate reader (Ex. 480, Em. 560, Varioskan LUX, Thermo scientific) and expressed as injected dose per gram of tissue (%ID/g). The calculation was based on calibration curves of Dox of known concentrations in the corresponding tissue individually.

2.8. In vivo treatment efficacy of subcutaneous HCT-116 tumor bearing mice

The treatment was started when the tumor reached about 50 mm^3, and this day was designated as day 0. The mice were divided into five groups randomly ($n = 5$) and *iv* injected with Lipo-Dox (4 mg Dox/kg), Ps-Dox (8 mg Dox/kg), or Tf@TBP-Ps-Dox (8 or 16 mg Dox/kg) and PBS (200 μL) every 4 days with total of 4 injections. Tumor volumes and body weights were monitored every two days, and both normalized to their initial values. All mice were sacrificed on day 20 after 2 injection cycles, and major organs and tumors were excised for photographs and

histological analyses. The tumor inhibition rate (TIR) was calculated: TIR (%) = (1 − tumor weight of treatment group/ tumor weight of PBS group) × 100. The tumors and major organs were fixed with 10% formalin solution, embedded in paraffin and sliced (thickness: 4 μm), and stained with hematoxylin and eosin (H&E) before observation with a digital microscope. The tumor slices were also subjected to terminal deoxynucleotidyl transferase-mediated nick end labeling (TUNEL) before CLSM observation (TCS SP5).

2.9. Statistical analyses

One-way ANOVA with Tukey multiple comparisons tests (Prism) were used to assess the difference between groups, wherein $^{*}p < .05$ was considered significant, $^{**}p < .01$ and $^{***}p < .001$ were highly significant.

3. Results and discussion

3.1. Formation and characterization of TBP-Ps-Dox and Tf@TBP-Ps-Dox

TBP-Ps-Dox with three different TBP molar surface densities were obtained from co-assembly of PEG-P(TMC-DTC) and 8.6, 17.2 and 25.8 mol% TBP-PEG-P(TMC-DTC) (referring to total copolymers), followed by Dox·HCl loading using a pH gradient method (Scheme 1A). To make TBP preferentially located at the outer surface of polymersomes facilitating the Tf binding, the PEG in TBP-PEG-P(TMC-DTC) (M_n = 7.5 kg/mol) was designed longer than that in PEG-P(TMC-DTC) (M_n = 5.0 kg/mol) (Table S1). The dynamic light scattering (DLS) revealed that all TBP-Ps-Dox exhibited small sizes around 72 nm with narrow polydispersity indexes (PDI) (Table 1), which were nearly identical to those of Ps-Dox fabricated from PEG-P(TMC-DTC) alone (*ca.* 70 nm). Moreover, all three TBP-Ps-Dox displayed a similar drug loading content (DLC = 9.4–9.6 wt%), indicating that TBP has negligible effect on both size and drug loading. TBP-Ps-Dox was robust during storage and against either extensive dilution or in the presence of 10% serum, resulting from the disulfide-crosslinking of polymersomal membrane during preparation as reported previously [40,45].

Tf@TBP-Ps-Dox was produced by incubating pre-formed TBP-Ps-Dox with Tf solutions followed by extensive dialysis to remove unbound Tf. First, the incubation at TBP/Tf = 1/1 (mol/mol) for 1 h led to Tf@TBP-Ps-Dox, and Tf binding had little influence on the size and size distribution (Fig. 1A). As anticipated, Tf surface contents of Tf@TBP-Ps-Dox accorded well with TBP surface densities (Fig. 1B). Tf@TBP-Ps-Dox with controllable Tf surface density of 1.6, 4.0 and 6.5 mol% could be fabricated. The Tf binding efficiency was *ca.* 25%. Due to the low amount of Tf on Tf@TBP-Ps-Dox, they exhibited only slightly more negative surface charge than TBP-Ps-Dox (Table 1). The static light scattering (SLS) measurements showed that polymersomes had an aggregation number of *ca.* 450 [46]. The number of TBP and transferrin on the surface of TBP-Ps-Dox (17.2 mol%) and Tf@TBP-Ps-Dox (4.0 mol %) were calculated to be *ca.* 77 and 18, respectively. It is noted that the affinity of TBP to Tf increased with increasing TBP surface density from 8.6% to 17.2% (Fig. S1A), likely due to a higher valency of TBP on the polymersome surface. Further increasing TBP density from 17.6% to 25.8% had little influence on Tf affinity. Second, the Tf surface content of Tf@TBP-Ps-Dox showed dependence on the incubation time of TBP-Ps-Dox with Tf solutions at a concentration of Tf in blood: a rapid binding at 10 min, a gradual increase at 30 min, and a decrease to a steady level after 1 h (Fig. S1B). This behavior was ascribed to the dynamic equilibrium of Tf binding to TBP-Ps-Dox. Therefore, Tf@TBP-Ps-Dox obtained by 1-h incubation was applied for following experiments.

Table 1
Characterizations of TBP-Ps-Dox with (Theoretical Dox loading content = 16.7 wt%)

Entry	TBP molar ratio (%)	Size (nm)[a]	PDI[a]	DLC[b] (wt%)	DLE[b] (%)	Zeta potential (mV)[c]	
						Without Tf	with Tf
1	8.6	73 ± 3	0.15	9.4	52%	−0.30	−0.89
2	17.2	72 ± 2	0.13	9.6	53%	0.41	−0.90
3	25.8	72 ± 3	0.16	9.4	52%	0.56	−1.83

[a] Determined by DLS.
[b] Drug loading content (DLC) and Drug loading efficiency (DLE) determined by UV–Vis spectroscopy.
[c] Determined by Zetasizer Nano-ZS equipped with a capillary electrophoresis cell before and after Tf binding.

To evaluate the stability of Tf binding to TBP-Ps, Tf was labeled with radioactive ^{125}I. The storage stability and exchange studies in Tf containing solutions displayed that over 85% ^{125}I-Tf (half-life of ^{125}I is 60.2 days) was retained on the polymersome surface when stored in PBS, in the presence of either 50-fold excess Tf, human serum or mouse whole blood for 48 h (Fig. 1C). These results illustrated that the Tf binding was quite stable and could not be replaced by Tf or other proteins in solution. This is in accordance with *ca.* 3 fold lower K_d of CGGGHKYLRW peptide binding to Tf (0.90 ± 0.25 μM) as compared to that to BSA (2.61 ± 0.38 μM) as reported by Signore [37].

3.2. TfR targeting and in vitro antitumor activity of Tf@TBP-Ps-Dox

Up-regulated TfR expresses on the surface of many cancerous cells like HCT-116 human colorectal cancer cells, MDA-MB 231 breast cancer cells and U87 MG glioblastoma cells [11,38,47,48]. It was reported that the expression of TfR on CRL-1831cells, a normal colon cell line was significantly lower than HCT-116 cells [38], and non-neoplastic breast cells had 4 to 5-fold lower TfR expression than malignant breast cells [49–51]. The TfR expression on HCT-116 cells were determined using CD71-PE antibody by flow cytometric analysis, taking MDA-MB 231 cells as positive control. Fig. S2 confirmed a high TfR expression on both HCT-116 and MDA-MB 231 cells. Here, we used HCT-116 cells for evaluating the *in vitro* and *in vivo* targeted delivery of Tf@TBP-Ps-Dox. Flow cytometric results indicated that Tf binding greatly enhanced the internalization of Ps-Dox, in which *ca.* 3-fold higher uptake was observed for Tf@TBP-Ps-Dox with TBP densities of 17.2 and 25.8 mol% (Fig. 2A). In comparison, Tf@TBP-Ps-Dox with 8.6 mol% TBP only showed little improvement. Davis et al. reported that there was a threshold of ligand contents for efficient TfR active targeting, and no significant difference in tumor accumulation was detected for gold nanoparticles with low ligand densities compared with non-targeting group [52]. Besides, our previous work on Tf modified Ps-Dox revealed a saturation of cellular uptake once Tf surface density beyond 3.9% [53]. Moreover, the cellular uptake of Tf@TBP-Ps-Dox was evidently inhibited by excess free Tf due to the competitive inhibition (Fig. 2B). Live cell imaging measurements displayed that Tf@TBP-Ps-Dox with 17.2 mol% TBP had faster and higher uptake (*ca.* 2.5-fold) by HCT-116 cells than Ps-Dox (Fig. S3&S4), supporting the active targeting effect of the Tf bound polymersomes. CLSM images of HCT-116 cells following 2 h incubation with Tf@TBP-Ps-Dox exhibited clearly more intensive Dox fluorescence than Ps-Dox (Fig. 2C). The homogenous distribution of Dox fluorescence inside the cells indicated the intracellular Dox release.

Of note, MTT assays of HCT-116 cells showed that blank Tf@TBP-Ps was non-toxic at 0.1–1 mg/mL (Fig. 3A), and the antitumor effect of Tf@TBP-Ps-Dox was strongly influenced by TBP densities. Tf@TBP-Ps-Dox with TBP densities of 17.2 mol% and 25.8 mol% caused greatly lowered cell viability than Tf@TBP-Ps-Dox with 8.6 mol% TBP, Ps-Dox and Lipo-Dox (Fig. 3B), which agrees well with the cell uptake results (Fig. 2A). The similar cytotoxic effect observed for Tf@TBP-Ps-Dox with TBP densities of 17.2 mol% and 25.8 mol% indicated that further increase in TBP had no beneficial effect. Hence, Tf@TBP-Ps-Dox with

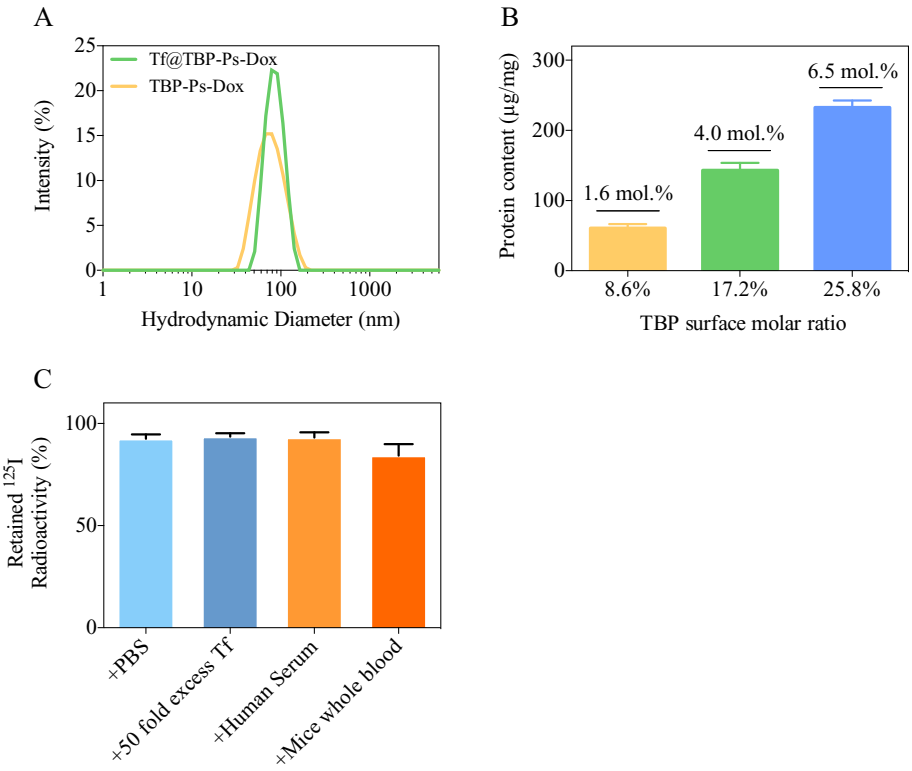

Fig. 1. (A) Size and size distribution of TBP-Ps-Dox and Tf@TBP-Ps-Dox determined by DLS. (B) Tf surface density corresponding to varying TBP density at TBP/Tf = 1/1 (mol/mol) as a function of TBP surface density. The numbers on top of the bars correspond to the Tf surface density. (C) The *in vitro* stability of Tf bound TBP-Ps studied using ^{125}I-labeled Tf against storage in PBS, 50-fold excess Tf, human serum, and mouse whole blood for 48 h, respectively. The retained ^{125}I radioactivity was obtained by comparing to the radioactivity of polymersomes taking into account 2-day attenuation.

17.2 mol% TBP was selected for further investigations. If not specified, Tf@TBP-Ps-Dox with 17.2 mol% TBP was used in the following studies.

The half-maximal inhibitory concentrations (IC_{50}) of Tf@TBP-Ps-Dox, Ps-Dox and Lipo-Dox were determined to be 1.4 ± 1.08, 3.5 ± 1.13 and 6.4 ± 1.09 μg Dox equiv./mL, respectively (Fig. 3C). In other words, Tf@TBP-Ps-Dox was *ca.* 2.5 and 4.5-fold more potent against HCT-116 cells than Ps-Dox and Lipo-Dox, respectively. Of note, Tf-functionalized liposomes, Tf-indocyane green assemblies, and Tf conjugated PLGA nanoparticles showed similar enhancement in cellular uptake and cytotoxicity in HCT-8 colon cancer cells and U87 MG cancer cells [11,48,54]. Live/dead assays showed clearly more apoptotic cells caused by Tf@TBP-Ps-Dox than by Ps-Dox (Fig. S5). In addition, the cytotoxicity of Tf@TBP-Ps-Dox to HCT-116 cells was greatly reduced at co-incubation with free Tf (Fig. 3D), supporting that the uptake of Tf@TBP-Ps-Dox by HCT-116 cells is mediated by TfR. These results confirm that Tf is stably bound on the surface of polymersomes and can effectively enhance the uptake of polymersomes in TfR over-expressing cancer cells.

3.3. The tumor accumulation and pharmacokinetics of Tf@TBP-Ps

To monitor the biodistribution of Tf@TBP-Ps in the subcutaneous HCT-116 colorectal tumor model using near-infrared imaging (NIR), Cy5 labeled Tf@TBP-Ps and Ps were applied. The *in vivo* imaging results showed fast and high accumulation of Tf@TBP-Ps in the tumor (Fig. 4A). The tumor exhibited the highest Cy5 fluorescence in the body and tumor Cy5 fluorescence increased from 2 to 8 h after *iv* administration. In contrast, the non-targeting Ps control exhibited much lower tumor accumulation, confirming the active HCT-116 tumor targeting of Tf@TBP-Ps. The *ex vivo* images of major organs and tumors at 24 h post-injection corroborated with enhanced tumor accumulation of Tf@TBP-Ps than TBP-Ps (Fig. 4B). The quantification of Dox in different tissues and tumors showed a tumor accumulation of 8.5% ID/g for Tf@TBP-Ps-Dox at 24 h post-injection, which was over 2-fold higher than Ps-Dox (Fig. 4C). There was a discrepancy in liver accumulation for Cy5-labeled polymersomes and Dox, which needs further investigation. Furthermore, the *in vivo* pharmacokinetics following *iv* injection with 8 mg Dox/kg displayed that both Tf@TBP-Ps-Dox and Ps-Dox had long circulation time. The elimination half-life and AUC of Tf@TBP-Ps-Dox were determined to be 9.5 h and 10 μg/mL·h, respectively, while those of Ps-Dox were 8.9 h and 8.7 μg/mL·h, respectively (Fig. 4D). Thus, the binding of TBP-Ps-Dox to Tf will not lead to detrimental effect to its stability and circulation *in vivo*. The pharmacokinetics of Tf@TBP-Ps-Dox might be somewhat different in tumor-bearing mice. It is noted that *iv* administration of targeted nanoformulations may lead to the formation of protein corona at the surface, which would significantly reduce their targetability. The selective binding of circulating Tf in the blood to TBP-Ps-Dox upon injection might lessen the formation of protein corona. On the other hand, the presence of abundant endogenous Tf in circulation might also result in competitive inhibition with Tf@TBP-Ps-Dox toward TfR. We will carry out systematic studies to clarify this in the future.

3.4. Targeted treatment of subcutaneous HCT-116 tumor in mice

The antitumor efficacy of Tf@TBP-Ps-Dox was studied in subcutaneous HCT-116 tumor model when tumor volume reached 50 mm^3. Tf@TBP-Ps-Dox was *iv* injected every 4 days at 8 or 16 mg Dox/kg with a total of 4 injections. Ps-Dox (8 mg Dox/kg), Lipo-Dox (4 mg Dox/kg), and PBS were used as controls. Owing to its dose-limiting toxicity, Lipo-Dox was given at 4 mg Dox/kg [53]. Fig. 5A shows that Tf@TBP-Ps-Dox instigated significantly more effective tumor inhibition at 8 mg Dox/kg than Ps-Dox, supporting that Tf binding plays an important role in tumor treatment. Notably, tumor inhibition was further enhanced for Tf@TBP-Ps-Dox at 16 mg Dox/kg (*$p < .05$). Lipo-Dox presented similar tumor inhibition to Tf@TBP-Ps-Dox at 8 mg Dox/kg, which was possibly due to the fast internalization and/or drug release upon cell membrane fusion of Lipo-Dox. However, the mice revealed hand-foot syndrome (HFS) and significant body weight loss during the treatment (**$p < .01$). In contrast, HFS and weight loss did not occur for both Tf@TBP-Ps-Dox groups and Ps-Dox (Fig. 5B), confirming the low systemic toxicity of polymersomal Dox. This corroborates well to the high

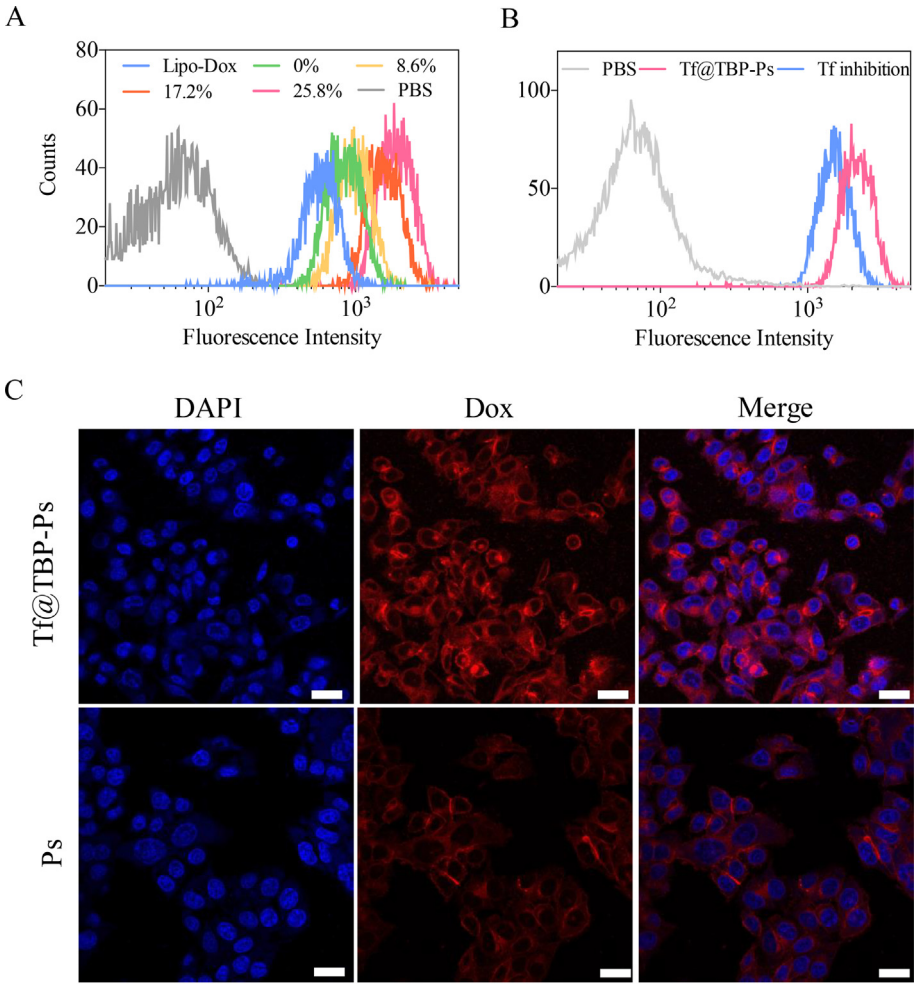

Fig. 2. (A) Flow cytometry measurements of HCT-116 cells incubated 2 h with Tf@TBP-Ps-Dox with variable TBP surface densities. Lipo-Dox and PBS were used as controls. (B) HCT-116 cell uptake studies of Tf@TBP-Ps-Dox with or without 0.5 mM free Tf inhibition by flow cytometry. (C) Intracellular Dox release from Tf@TBP-Ps-Dox and Ps-Dox observed by CLSM. Scale Bar: 25 μm.

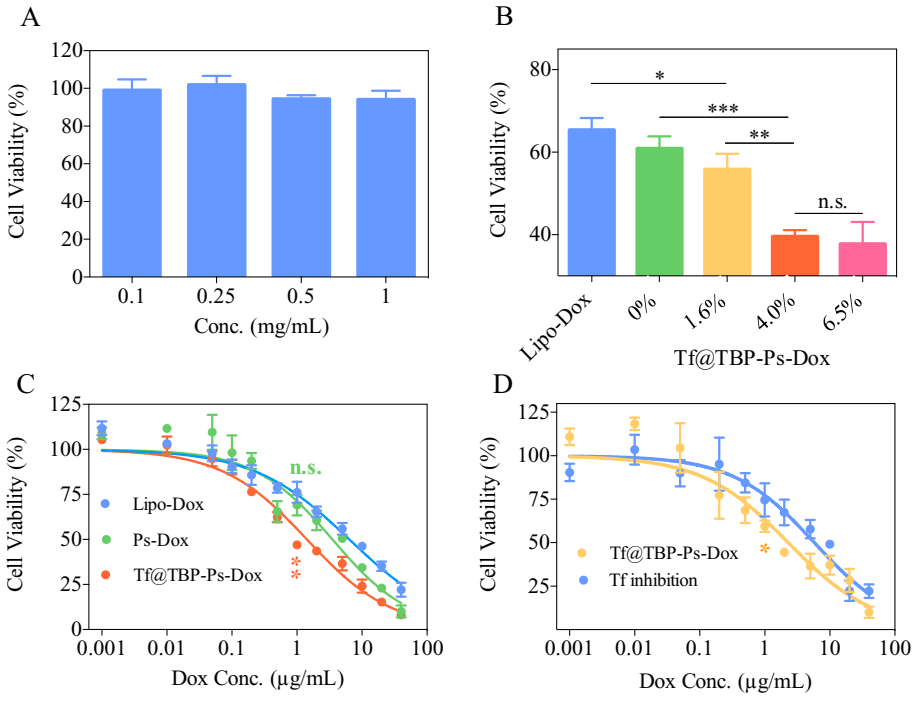

Fig. 3. (A) Cytotoxicity of blank Tf@TBP-Ps determined by MTT assays. (B) Viability of HCT-116 cells after 2 h treatment with Tf@TBP-Ps-Dox (2 μg Dox/mL) and 70 h incubation with fresh medium. TBP densities varied from 8.6%, 17.2% to 25.8 mol %. (C) Dependence of HCT-116 cell viability on concentrations of Tf@TBP-Ps-Dox with 17.2% TBP. Ps-Dox and Lipo-Dox were used as controls. (D) Competitive inhibition experiments performed on Tf@TBP-Ps-Dox in HCT-116 cells by MTT assays. Data are presented as mean ± SD (n = 5). Statistical analyses: one-way Anova Tukey multiple comparisons tests (for B) and student t-test (for C and D), $^{*}p < .05$, $^{**}p < .01$, $^{***}p < .001$.

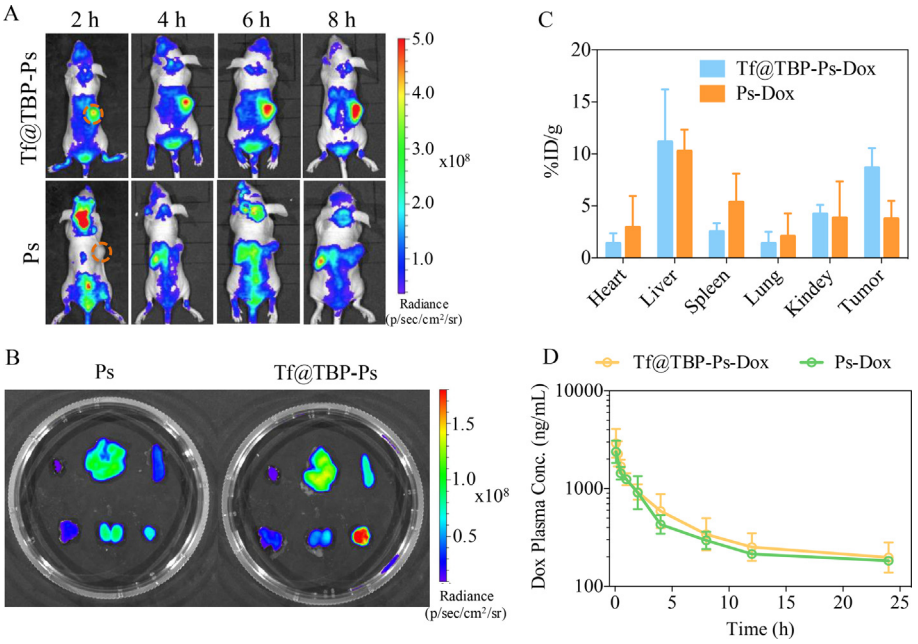

Fig. 4. (A) *In vivo* imaging of HCT-116 tumor-bearing mice after *i.v.* injection of Cy5-labeled Tf@TBP-Ps and Ps. The orange circles indicate the tumor regions. (B) The *ex vivo* images of major organs and tumor of mice at 24 h after injection with Cy5-labeled Tf@TBP-Ps and Ps. (C) The DOX biodistribution in HCT-116 tumor-bearing mice at 24 h after *iv* injecting with Tf@TBP-Ps-Dox and Ps-Dox (8 mg Dox/kg). (D) Pharmacokinetics of Tf@TBP-Ps-Dox and Ps-Dox in healthy Balb/c mice (8 mg Dox/kg).

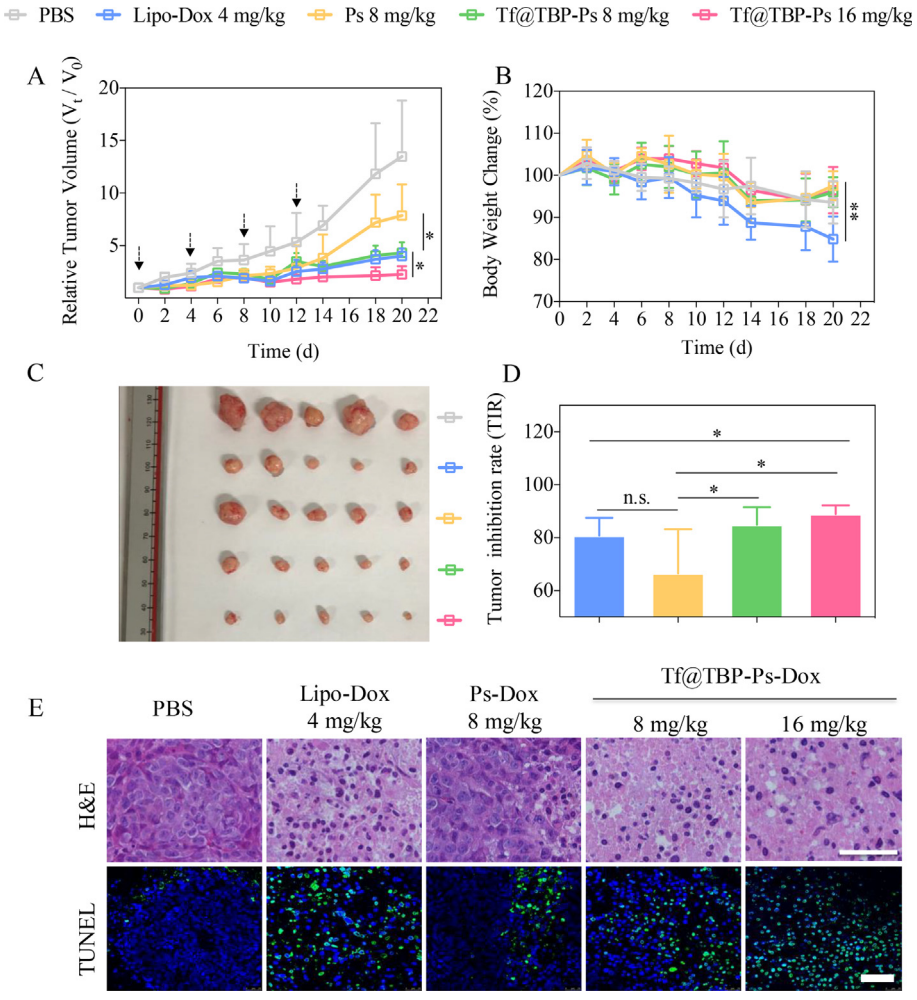

Fig. 5. *In vivo* antitumor efficacy of Tf@TBP-Ps-Dox at 8 or 16 mg Dox/kg in HCT-116 tumor-bearing nude mice (n = 5). Ps-Dox (8 mg Dox/kg), Lipo-Dox (4 mg Dox/kg) and PBS were used as controls. The drug was given on day 0, 4, 8, and 12. (A) Tumor volume changes. (B) Body weight changes. (C) Photographs of tumors collected on day 20. (D) Tumor inhibition rates of different groups on day 20. (E) H&E and TUNEL assays of tumor tissues on day 20. Scale bars: 50 μm. For A, B and D, data are presented as mean ± SD (n = 5) and one-way Anova and Tukey multiple comparisons tests was applied, *p < .05, **p < .01.

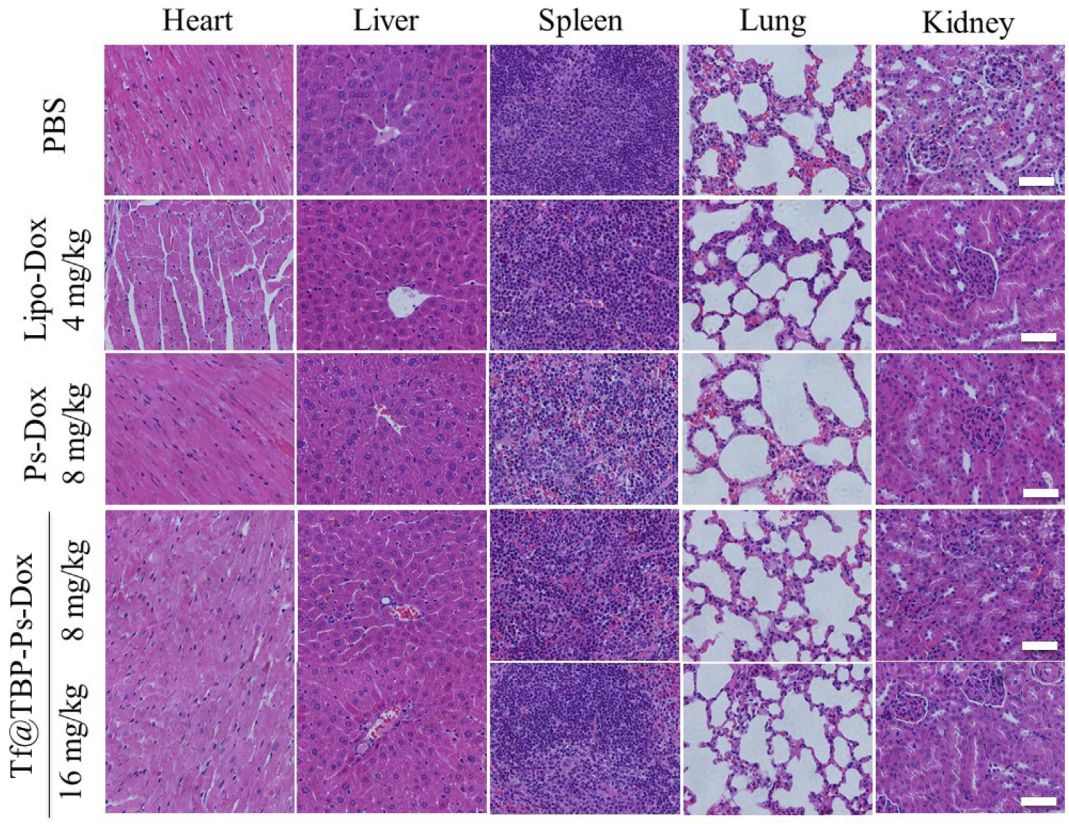

Fig. 6. H&E stained heart, liver, spleen, lung and kidney tissues excised from tumor bearing mice following 20 d treatment. Scale bars: 50 μm.

maximum-tolerated dose of Ps-Dox of over 100 mg Dox/kg [40]. Moreover, on day 20 the mice were sacrificed, and the tumors of Tf@TBP-Ps-Dox at 16 mg Dox/kg were the smallest among all groups (Fig. 5C). Notably, Tf@TBP-Ps-Dox revealed a tumor inhibition rate (TIR) of 89% at 16 mg Dox/kg and 84% at 8 mg Dox/kg, which were significantly better than Ps-Dox (TIR 66%) and Lipo-Dox (Fig. 5D). Furthermore, H&E staining of tumor tissues exhibited that the two Tf@TBP-Ps-Dox groups caused massive cell apoptosis: nucleus dissolution and fragmentation with concurrent cell shrinkage showing very dense alkaline staining due to chromosome compression. In comparison, the extent of apoptosis and necrosis caused by Lipo-Dox was lower, and Ps-Dox induced significantly less apoptosis (Fig. 5E). TUNEL assays demonstrated that Tf@TBP-Ps-Dox and Lipo-Dox groups had much less cells and produced more pronounced tumor cell apoptosis than Ps-Dox (Fig. 5E). No severe side effects in major organs were found from the histological analysis after Tf@TBP-Ps-Dox treatment (Fig. 6). These results conclude that Tf@TBP-Ps-Dox is much safer and causes less toxic effects and better tumor suppression at 16 mg Dox/kg than Lipo-Dox at 4 mg Dox/kg. The antitumor efficacy of Tf@TBP-Ps-Dox is dose-dependent, as evidenced by significantly better tumor inhibition at 16 mg Dox/kg over 8 mg Dox/kg. Ps-Dox was reported to possess a remarkable maximum-tolerated dose of > 100 mg Dox/kg [40]. Given its high therapeutic index, dose escalation of Tf@TBP-Ps-Dox might further increase the treatment efficacy. In contrast, Lipo-Dox gave already pronounced toxicity at 4 mg Dox/kg, which deters dose escalation.

4. Conclusion

We have demonstrated that disulfide-crosslinked polymersomes functionalized with a transferrin-binding peptide (TBP-Ps) can selectively and stably bind transferrin and subsequently mediate targeted Dox delivery to TfR over-expressing HCT-116 colorectal cancer cells *in vitro* and *in vivo*, leading to enhanced tumor suppression and reduced off-target side effects. To the best of our knowledge, this is the first report on the preparation of transferrin-functionalized nanomedicines by selective binding of transferrin. This transferrin-binding strategy is robust and has greatly simplified the production of transferrin-functionalized nanomedicines. Of note, the present study has employed a xenografted HCT-116 colorectal cancer model. We will investigate the antitumor effect of TBP-Ps-Dox using allograft models, *i.e. via* binding endogenous transferrin in the blood. This proof-of-concept study has shown that the surface modification of nanoparticles with Tf-binding peptide provides an appealing strategy in formulating Tf-targeted nanomedicines.

Acknowledgements

This work is supported by research grants from the National Natural Science Foundation of China (NSFC 51633005, 51761135117, 51773146, 51861145310, 51561135010).

Appendix A. Supplementary data

Supplementary data to this article can be found online at https://doi.org/10.1016/j.jconrel.2020.01.012.

References

[1] J.J. Shi, P.W. Kantoff, R. Wooster, O.C. Farokhzad, Cancer nanomedicine: progress, challenges and opportunities, Nat. Rev. Cancer 17 (2017) 20–37.
[2] Y.Q. Zhu, J. Feijen, Z.Y. Zhong, Dual-targeted nanomedicines for enhanced tumor treatment, Nano Today 18 (2018) 65–85.
[3] J.L. Markman, A. Rekechenetskiy, E. Holler, J.Y. Ljubimova, Nanomedicine therapeutic approaches to overcome cancer drug resistance, Adv. Drug Deliv. Rev. 65 (2013) 1866–1879.
[4] A. Anitha, S. Maya, A.J. Sivaram, U. Mony, R. Jayakumar, Combinatorial nanomedicines for colon cancer therapy, Wiley Interdiscip. Rev.-Nanomed.

Nanobiotechnol. 8 (2016) 151–159.
[5] H.L. Sun, Y.Y. Dong, F.J. Jan, Z.Y. Zhong, Peptide-decorated polymeric nanomedicines for precision cancer therapy, J. Control. Release 290 (2018) 11–27.
[6] E. Ruoslahti, Tumor penetrating peptides for improved drug delivery, Adv. Drug Deliv. Rev. 110 (2017) 3–12.
[7] J.M. Montenegro, V. Grazu, A. Sukhanova, S. Agarwal, J.M. de la Fuente, I. Nabiev, A. Greiner, W.J. Parak, Controlled antibody/(bio-) conjugation of inorganic nanoparticles for targeted delivery, Adv. Drug Deliv. Rev. 65 (2013) 677–688.
[8] A. Alibakhshi, F.A. Kahaki, S. Ahangarzadeh, H. Yaghoobi, F. Yarian, R. Arezumand, J. Ranjbari, A. Mokhtarzadeh, M. de la Guardia, Targeted cancer therapy through antibody fragments-decorated nanomedicines, J. Control. Release 268 (2017) 323–334.
[9] M.S. Muthu, R.V. Kutty, Z.T. Luo, J.P. Xie, S.S. Feng, Theranostic vitamin E TPGS micelles of transferrin conjugation for targeted co-delivery of docetaxel and ultra bright gold nanoclusters, Biomaterials 39 (2015) 234–248.
[10] J. Zhou, M.H. Li, W.Q. Lim, Z. Luo, S.Z.F. Phua, R.L. Huo, L.Q. Li, K. Li, L.L. Dai, J.J. Liu, K.Y. Cai, Y.L. Zhao, A transferrin-conjugated hollow Nanoplatform for redox-controlled and targeted chemotherapy of tumor with reduced inflammatory reactions, Theranostics 8 (2018) 518–532.
[11] Y. Cui, Q. Xu, P.K.-H. Chow, D. Wang, C.-H. Wang, Transferrin-conjugated magnetic silica PLGA nanoparticles loaded with doxorubicin and paclitaxel for brain glioma treatment, Biomaterials 34 (2013) 8511–8520.
[12] S.K. Sriraman, G. Salzano, C. Sarisozen, V. Torchilin, Anti-cancer activity of doxorubicin-loaded liposomes co-modified with transferrin and folic acid, Eur. J. Pharm. Biopharm. 105 (2016) 40–49.
[13] W. Cheng, J.P. Nie, L. Xu, C.Y. Liang, Y. Peng, G. Liu, T. Wang, L. Mei, L.Q. Huang, X.W. Zeng, pH-sensitive delivery vehicle based on folic acid-conjugated polydopamine-modified mesoporous silica nanoparticles for targeted cancer therapy, ACS Appl. Mater. Interfaces 9 (2017) 18462–18473.
[14] M. Talelli, M. Barz, C.J.F. Rijcken, F. Kiessling, W.E. Hennink, T. Lammers, Core-crosslinked polymeric micelles: principles, preparation, biomedical applications and clinical translation, Nano Today 10 (2015) 93–117.
[15] A. Wicki, D. Witzigmann, V. Balasubramanian, J. Huwyler, Nanomedicine in cancer therapy: challenges, opportunities, and clinical applications, J. Control. Release 200 (2015) 138–157.
[16] Y.S. Youn, Y.H. Bae, Perspectives on the past, present and future of cancer nanomedicine, Adv. Drug Deliv. Rev. 130 (2018) 3–11.
[17] R. van der Meel, L.J.C. Vehmeijer, R.J. Kok, G. Storm, E.V.B. van Gaal, Ligand-targeted particulate nanomedicines undergoing clinical evaluation: current status, Adv. Drug Deliv. Rev. 65 (2013) 1284–1298.
[18] K.F. Pirollo, J. Nemunaitis, P.K. Leung, R. Nunan, J. Adams, E.H. Chang, Safety and efficacy in advanced solid tumors of a targeted nanocomplex carrying the p53 gene used in combination with docetaxel: a phase 1b study, Mol. Ther. 24 (2016) 1697–1706.
[19] A. Siefker-Radtke, X.Q. Zhang, C.C. Guo, Y. Shen, K.F. Pirollo, S. Sabir, C. Leung, C. Leong-Wu, C.M. Ling, E.H. Chang, R.E. Millikan, W.F. Benedict, A phase l study of a tumor-targeted systemic nanodelivery system, SGT-94, in genitourinary cancers, Mol. Ther. 24 (2016) 1484–1491.
[20] R. Singh, M. Norret, M.J. House, Y. Galabura, M. Bradshaw, D.W. Ho, R.C. Woodward, T.G.S. Pierre, I. Luzinov, N.M. Smith, L.Y. Lim, K.S. Iyer, Dose-dependent therapeutic distinction between active and passive targeting revealed using transferrin-coated PGMA nanoparticles, Small 12 (2016) 351–359.
[21] S. Ruan, L. Qin, W. Xiao, C. Hu, Y. Zhou, R. Wang, X. Sun, W. Yu, Q. He, H. Gao, Acid-responsive transferrin dissociation and GLUT mediated exocytosis for increased blood-brain barrier transcytosis and programmed glioma targeting delivery, Adv. Funct. Mater. 28 (2018).
[22] F.C. Lam, S.W. Morton, J. Wyckoff, T.L. Vu Han, M.K. Hwang, A. Maffa, E. Balkanska-Sinclair, M.B. Yaffe, S.R. Floyd, P.T. Hammond, Enhanced efficacy of combined temozolomide and bromodomain inhibitor therapy for gliomas using targeted nanoparticles, Nat. Commun. 9 (2018) 1991.
[23] L. Liu, Y. Wei, S. Zhai, Q. Chen, D. Xing, Dihydroartemisinin and transferrin dual-dressed nano-graphene oxide for a pH-triggered chemotherapy, Biomaterials 62 (2015) 35–46.
[24] S.S. Kim, A. Rait, E. Kim, J. DeMarco, K.F. Pirollo, E.H. Chang, Encapsulation of temozolomide in a tumor-targeting nanocomplex enhances anti-cancer efficacy and reduces toxicity in a mouse model of glioblastoma, Cancer Lett. 369 (2015) 250–258.
[25] S.S. Kim, A. Rait, F. Rubab, A.K. Rao, M.C. Kiritsy, K.F. Pirollo, S. Wang, L.M. Weiner, E.H. Chang, The clinical potential of targeted nanomedicine: delivering to cancer stem-like cells, Mol. Ther. 22 (2014) 278–291.
[26] N.C. Bellocq, S.H. Pun, G.S. Jensen, M.E. Davis, Transferrin-containing, cyclodextrin polymer-based particles for tumor-targeted gene delivery, Bioconjug. Chem. 14 (2003) 1122–1132.
[27] M.E. Davis, J.E. Zuckerman, C.H.J. Choi, D. Seligson, A. Tolcher, C.A. Alabi, Y. Yen, J.D. Heidel, A. Ribas, Evidence of RNAi in humans from systemically administered siRNA via targeted nanoparticles, Nature 464 (2010) 1067–1070.
[28] N. Senzer, J. Nemunaitis, D. Nemunaitis, C. Bedell, G. Edelman, M. Barve, R. Nunan, K.F. Pirollo, A. Rait, E.H. Chang, Phase I study of a systemically delivered p53 nanoparticle in advanced solid tumors, Mol. Ther. 21 (2013) 1096–1103.
[29] J.-J. Hu, D. Xiao, X.-Z. Zhang, Advances in peptide functionalization on mesoporous silica nanoparticles for controlled drug release, Small 12 (2016) 3344–3359.
[30] H. Jin, J. Pi, Y. Zhao, J.H. Jiang, T. Li, X.Y. Zeng, P.H. Yang, C.E. Evans, J.Y. Cai, EGFR-targeting PLGA-PEG nanoparticles as a curcumin delivery system for breast cancer therapy, Nanoscale 9 (2017) 16365–16374.
[31] A.M. Brinkman, G.J. Chen, Y.D. Wang, C.J. Hedman, N.M. Sherer, T.C. Havighurst, S.Q. Gong, W. Xu, Aminoflavone-loaded EGFR-targeted unimolecular micelle nanoparticles exhibit anti-cancer effects in triple negative breast cancer, Biomaterials 101 (2016) 20–31.
[32] X.W. Cheng, D.R. Yu, G. Cheng, B.C. Yung, Y. Liu, H.W. Li, C. Kang, X.Y. Fang, S.H. Tian, X.J. Zhou, Q.B. Liu, R.J. Lee, T7 peptide-conjugated lipid nanoparticles for dual modulation of Bcl-2 and Akt-1 in lung and cervical carcinomas, Mol. Pharm. 15 (2018) 4722–4732.
[33] Y. Kuang, K.C. Zhang, Y. Cao, X. Chen, K.W. Wang, M. Liu, R.J. Pei, Hydrophobic IR-780 dye encapsulated in cRGD-conjugated solid lipid nanoparticles for NIR imaging-guided photothermal therapy, ACS Appl. Mater. Interfaces 9 (2017) 12217–12226.
[34] Q.F. Zhao, H.J. Geng, Y. Wang, Y.K. Gao, J.H. Huang, Y. Wang, J.H. Zhang, S.L. Wang, Hyaluronic acid oligosaccharide modified redox-responsive mesoporous silica nanoparticles for targeted drug delivery, ACS Appl. Mater. Interfaces 6 (2014) 20290–20299.
[35] J. Lee, E.T. Oh, M.H. Choi, H.G. Kim, H.J. Park, C. Kim, Dual-functional cyclic peptide switch on mesoporous nanocontainers for selective CD44 targeting and on-off gatekeeping triggered by conformational transformation, New J. Chem. 42 (2018) 12938–12944.
[36] D.D. Von Hoff, M.M. Mita, R.K. Ramanathan, G.J. Weiss, A.C. Mita, P.M. LoRusso, H.A. Burris, L.L. Hart, S.C. Low, D.M. Parsons, S.E. Zale, J.M. Summa, H. Youssoufian, J.C. Sachdev, Phase I study of PSMA-targeted docetaxel-containing nanoparticle BIND-014 in patients with advanced solid tumors, Clin. Cancer Res. 22 (2016) 3157–3163.
[37] M. Santi, G. Maccari, P. Mereghetti, V. Voliani, S. Rocchiccioli, N. Ucciferri, S. Luin, G. Signore, Rational design of a transferrin-binding peptide sequence tailored to targeted nanoparticle internalization, Bioconjug. Chem. 28 (2017) 471–480.
[38] H. Makwana, F. Mastrotto, J.P. Magnusson, D. Sleep, J. Hay, K.J. Nicholls, S. Allen, C. Alexander, Engineered polymer-transferrin conjugates as self-assembling targeted drug delivery systems, Biomacromolecules 18 (2017) 1532–1543.
[39] R.L. Siegel, K.D. Miller, S.A. Fedewa, D.J. Ahnen, R.G.S. Meester, A. Barzi, A. Jemal, Colorectal cancer statistics, 2017, CA-Cancer J. Clin. 67 (2017) 177–193.
[40] Y. Zou, F.H. Meng, C. Deng, Z.Y. Zhong, Robust, tumor-homing and redox-sensitive polymersomal doxorubicin: a superior alternative to Doxil and Caelyx? J. Control. Release 239 (2016) 149–158.
[41] Y. Fang, W.J. Yang, L. Cheng, F.H. Meng, J. Zhang, Z.Y. Zhong, EGFR-targeted multifunctional polymersomal doxorubicin induces selective and potent suppression of orthotopic human liver cancer in vivo, Acta Biomater. 64 (2017) 323–333.
[42] N. Zhang, Y.F. Xia, Y. Zou, W.J. Yang, J. Zhang, Z.Y. Zhong, F.H. Meng, ATN-161 peptide functionalized reversibly cross-linked polymersomes mediate targeted doxorubicin delivery into melanoma-bearing C57BL/6 mice, Mol. Pharm. 14 (2017) 2538–2547.
[43] Y. Zou, Y.F. Xia, F.H. Meng, J. Zhang, Z.Y. Zhong, GE11-directed functional polymersomal doxorubicin as an advanced alternative to clinical liposomal formulation for ovarian cancer treatment, Mol. Pharm. 15 (2018) 3664–3671.
[44] Y. Zhu, J. Zhang, F.H. Meng, C. Deng, R. Cheng, J. Feijen, Z.Y. Zhong, cRGD-functionalized reduction-sensitive shell-sheddable biodegradable micelles mediate enhanced doxorubicin delivery to human glioma xenografts in vivo, J. Control. Release 233 (2016) 29–38.
[45] W.J. Yang, Y.H. Wei, L. Yang, J. Zhang, Z.Y. Zhong, G. Storm, F.H. Meng, Granzyme B-loaded, cell-selective penetrating and reduction-responsive polymersomes effectively inhibit progression of orthotopic human lung tumor in vivo, J. Control. Release 290 (2018) 141–149.
[46] L. Ding, W. Gu, Y. Zhang, S. Yue, H. Sun, J.J. Cornelissen, Z.J.B. Zhong, HER2-specific reduction-sensitive immunopolymersomes with high loading of Epirubicin for targeted treatment of ovarian tumor, Biomacromolecules 20 (2019) 3855–3863.
[47] M.S. Muthu, R.V. Kutty, Z. Luo, J. Xie, S.S. Feng, Theranostic vitamin E TPGS micelles of transferrin conjugation for targeted co-delivery of docetaxel and ultra bright gold nanoclusters, Biomaterials 39 (2015) 234–248.
[48] M. Zhu, Z. Sheng, Y. Jia, D. Hu, X. Liu, X. Xia, C. Liu, P. Wang, X. Wang, H. Zheng, Indocyanine green-holo-transferrin nanoassemblies for tumor-targeted dual-modal imaging and photothermal therapy of glioma, ACS Appl. Mater. Interfaces 9 (2017) 39249–39258.
[49] H.O. Habashy, D.G. Powe, C.M. Staka, E.A. Rakha, G. Ball, A.R. Green, M. Aleskandarany, E.C. Paish, R.D. Macmillan, R.I. Nicholson, I.O. Ellis, J.M.W. Gee, Transferrin receptor (CD71) is a marker of poor prognosis in breast cancer and can predict response to tamoxifen, Breast Cancer Res. Treat. 119 (2010) 283–293.
[50] S.E. Tonik, J.E. Shindelman, H.H. Sussman, Transferrin receptor is inversely correlated with estrogen-receptor in breast-cancer, Breast Cancer Res. Treat. 7 (1986) 71–76.
[51] R.A. Walker, S.J. Day, Transferrin receptor expression in non-malignant and malignant human breast tissue, J. Pathol. 148 (1986) 217–224.
[52] C.H.J. Choi, C.A. Alabi, P. Webster, M.E. Davis, Mechanism of active targeting in solid tumors with transferrin-containing gold nanoparticles, Proc. Natl. Acad. Sci. U. S. A. 107 (2010) 1235–1240.
[53] Y. Wei, X. Gu, L. Cheng, F. Meng, G. Storm, Z. Zhong, Low-toxicity transferrin-guided polymersomal doxorubicin for potent chemotherapy of orthotopic hepatocellular carcinoma in vivo, Acta Biomater. 92 (2019) 196–204.
[54] I. Leto, M. Coronnello, C. Righeschi, M.C. Bergonzi, E. Mini, A.R. Bilia, Enhanced efficacy of artemisinin loaded in transferrin-conjugated liposomes versus stealth liposomes against HCT-8 Colon cancer cells, ChemMedChem 11 (2016) 1745–1751.